

# A Low-Memory Implementation of Perfectly Matched Layers with Smooth-Varying Coefficients in Discontinuous Galerkin Time Domain Methods

Liang Chen, Mehmet Burak Ozakin, and Hakan Bagci

## Abstract

The perfectly matched layer (PML) is one of the most popular domain truncation techniques used in differential-equation based wave-type equation solvers. Practical implementations of PMLs often use smooth-varying attenuation coefficients to reduce the numerical reflection from PMLs and to reduce the thickness required for reaching a certain level of absorption. In discontinuous Galerkin time-domain (DGTD) methods, assigning smooth-varying coefficients calls for storing individual mass matrices for each mesh element, which significantly increases the memory-cost. This work proposes a memory-efficient implementation of smooth-varying PMLs in DGTD. A weight-adjusted approximation is applied to the mass matrices involved in the PML formulation, which yields a low memory-cost algorithm and maintains the high-order accuracy of DGTD. The proposed scheme has the same accuracy as the implementation of storing local mass matrices of each element, and provides a higher mesh flexibility and a smaller reflection than using a constant coefficient in each element.

## Index Terms

Absorbing boundary condition, discontinuous Galerkin method, electromagnetic wave, perfectly matched layer, weight-adjusted approximation.

## I. INTRODUCTION

The perfectly matched layer (PML) is one of the most popular techniques used for domain truncation in differential-equation based wave-type equation solvers [1], [2]. Popular solvers include finite difference methods [3], finite element methods [4], and more recently-developed discontinuous Galerkin time domain method (DGTD) [5]–[10]. This work studies the implementation of PMLs in DGTD, in particular, for Maxwell equations. It is well-known that the performance of PML critically depends on the profile of the attenuation coefficient, i.e., the conductivity in Maxwell equations. To produce high absorption, the PML ideally requires a high conductivity value and/or has to be thick. But, in practice, one cannot either use a constant high conductivity as it would increase the numerical reflection at the PML interface (between the solution domain and the PML) or increase the thickness too much as it would result in high computational costs. Therefore, a smoothly increasing conductivity profile is often used for achieving both high absorption and small numerical reflection [1]–[4], [11]–[13].

The authors are with the Division of Computer, Electrical, and Mathematical Science and Engineering, King Abdullah University of Science and Technology (KAUST), Thuwal 23955-6900, Saudi Arabia (e-mail: liang.chen@kaust.edu.sa).

This work is supported by the King Abdullah University of Science and Technology (KAUST) Office of Sponsored Research (OSR) under Award No 2016-CRG5-2953.

The authors would like to thank the KAUST Supercomputing Laboratory (KSL) for providing the required computational resources.

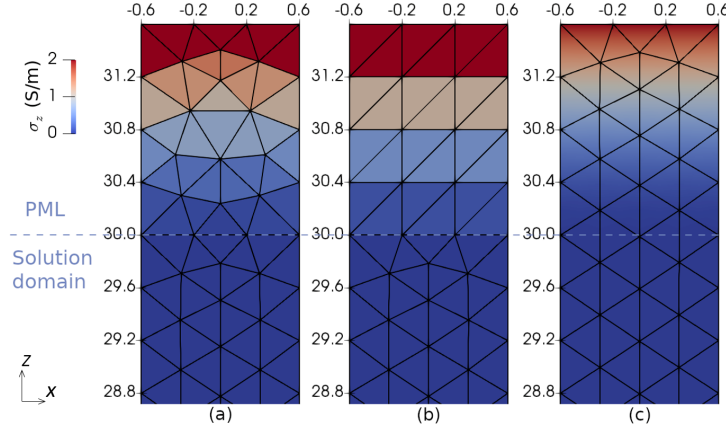


Fig. 1. Illustration of the PML conductivity profile. (a) EC with a paved mesh. (b) EC with a layered mesh. (c) SV with a paved mesh.

In DGTD, the conductivity profile can be implemented in two different ways. The first method considers the conductivity as element-wise constant (EC). Implementing EC conductivity in DGTD is straightforward since the mass matrices of different elements only differ by a constant (for linear elements) [8]. However, the EC profile introduces conductivity discontinuity between neighboring elements, as illustrated in Fig. 1 (a). The material interfaces that are not parallel to the PML interface lead to large reflections and destroy the high-order accuracy of the solution. One workaround is to build layered meshes, see Fig. 1 (b), or use orthogonal meshes [7], for the PMLs and accordingly set a layered conductivity profile. But this significantly complicates the preprocessing as one needs to control the mesh/conductivity on all edges and corners. Moreover, to reduce the numerical reflection, more PML layers are needed for reducing the conductivity jump between neighboring layers.

The second method considers a smooth-varying (SV) profile, where the conductivity varies inside each element. The high-order accuracy of DGTD provides the ability of accounting for material properties varying at the sub-elemental level. In this case, the PML behavior is solely determined by the conductivity value and the mesh interfaces can be aligned arbitrarily, see Fig. 1 (c). Besides, the SV profile can improve the performance of PML [14]–[16]. The main issue with implementing SV profile is the high memory-cost caused by the element-dependent mass matrix. A direct implementation requires storing the mass matrix (or its inverse) of each element [7], [9], [14], [15], [17], which increases the memory-cost substantially. For example, for the stretched-coordinate (SC)-PML [9], the memory-cost for storing the mass matrix is  $15K_{\text{PML}} \times N_p^2$  floating-point numbers (FPNs), where  $N_p$  is the number of interpolating nodes in each element,  $K_{\text{PML}}$  is the number of elements in PML, 15 comes from the 5 material-dependent coefficients in the update equations and 3 Cartesian components of the vector field. In contrast, for the EC case, since the reference mass matrix is used, only the constant conductivity of each element is stored, costing  $K_{\text{PML}}$  FPNs.

This work proposes a memory-efficient implementation of SC-PML with smooth-varying coefficients in DGTD. The proposed method considers the local variation of the conductivity in each element and approximates the local mass matrix with a weight-adjusted approximation (WAA) [18]. The WAA has been proved to be energy-stable and

preserve the high-order convergence of DGTD [18]–[20]. The resulting WAA formulation of SC-PML can be easily adapted to the classical matrix-free DG framework [8]. Compared with the direct implementation using local mass matrices, the proposed formulation reduces the memory-cost to  $15K_{\text{PML}} \times N_q$  FPNs, where  $N_q \sim N_p$ , while the PML performance retains the same. Numerical examples also show that the proposed SV profile implementation performs better than the EC profile and shows high-order convergence.

## II. FORMULATION

### A. WAA-DGTD for SC-PML

Start from the modified Maxwell equations with stretched-coordinates in a source-free and lossless media [2]

$$-j\omega\mu\mathbf{H} = \nabla_e \times \mathbf{E} \quad (1)$$

$$j\omega\epsilon\mathbf{E} = \nabla_h \times \mathbf{H} \quad (2)$$

where  $E$  and  $H$  are electric and magnetic field, respectively,  $\epsilon$  and  $\mu$  are permittivity and permeability, respectively,  $\omega$  is frequency, and

$$\nabla_e = \nabla_h = \hat{x} \frac{1}{s_x} \frac{\partial}{\partial x} + \hat{y} \frac{1}{s_y} \frac{\partial}{\partial y} + \hat{z} \frac{1}{s_z} \frac{\partial}{\partial z}. \quad (3)$$

The coordinate-stretching variables  $s_u$  are defined as [2], [9], [13]

$$s_u(u) = \kappa_u(u) + \frac{\sigma_u(u)}{j\omega\epsilon_0} \quad (4)$$

where  $\kappa_u$  and  $\sigma_u$  are one-dimensional positive real functions along the  $u$ -direction,  $u = x, y, z$ . Here,  $\sigma_u$  is the attenuation coefficient responsible for the wave absorption of SC-PML and  $\kappa_u$  changes the phase velocity of waves in SC-PML.

The update equations for fields in SC-CPML are [9]

$$\partial_t \ddot{a} \cdot \mu \mathbf{H} = -\nabla \times \mathbf{E} - \ddot{b} \cdot \mu \mathbf{H} - \ddot{c} \cdot \mu \mathbf{P}^H \quad (5)$$

$$\partial_t \ddot{a} \cdot \epsilon \mathbf{E} = \nabla \times \mathbf{H} - \ddot{b} \cdot \epsilon \mathbf{E} - \ddot{c} \cdot \mu \mathbf{P}^E \quad (6)$$

$$\partial_t \mathbf{P}^H = \ddot{\kappa}^{-1} \mathbf{H} - \ddot{d} \mathbf{P}^H \quad (7)$$

$$\partial_t \mathbf{P}^E = \ddot{\kappa}^{-1} \mathbf{E} - \ddot{d} \mathbf{P}^E \quad (8)$$

where  $\mathbf{P}^E$  and  $\mathbf{P}^H$  are auxiliary variables introduced to help transforming (1)-(2) to the time-domain [9],  $\ddot{a}$ ,  $\ddot{b}$ ,  $\ddot{c}$ ,  $\ddot{d}$ , and  $\ddot{\kappa}$  are diagonal tensors defined by

$$\begin{aligned} a_{uu} &= \frac{\kappa_v \kappa_w}{\kappa_u}, b_{uu} = \frac{1}{\kappa_u \epsilon_0} (\sigma_v \kappa_w + \sigma_w \kappa_v - a_{uu} \sigma_u) \\ c_{uu} &= \frac{\sigma_v \sigma_w}{\epsilon_0^2} - b_{uu} \frac{\sigma_u}{\epsilon_0}, d_{uu} = \frac{\sigma_u}{\kappa_u \epsilon_0}, \kappa_{uu} = \kappa_u. \end{aligned} \quad (9)$$

Here and hereafter  $(u, v, w)$  follows the permutation  $(x, y, z) \rightarrow (y, z, x) \rightarrow (z, x, y)$ .

Following the standard procedure of discontinuous Galerkin methods [8], [9], discretize the simulation domain into  $K$  elements, then in each element, use the divergence theorem twice, expand the variables with polynomial

basis functions and apply Galerkin testing, one obtain the strong form of the semi-discrete system, which yields the following matrix representation

$$\partial_t \bar{H}_k = -(\bar{M}_k^a)^{-1} [\bar{M}_k^b \bar{H}_k + \bar{M}_k^c \bar{P}_k^H \mu_k^{-1} \bar{\mathbb{C}}_k(\bar{E}_k, \bar{E}_{k'}, \bar{H}_k, \bar{H}_{k'})] \quad (10)$$

$$\partial_t \bar{E}_k = -(\bar{M}_k^a)^{-1} [\bar{M}_k^b \bar{E}_k + \bar{M}_k^c \bar{P}_k^E \varepsilon_k^{-1} \bar{\mathbb{C}}_k(\bar{H}_k, \bar{H}_{k'}, \bar{E}_k, \bar{E}_{k'})] \quad (11)$$

$$\partial_t \bar{P}_k^H = \bar{M}_k^{-1} (\bar{M}_k^{\kappa^{-1}} \bar{H}_k - \bar{M}_k^d \bar{P}_k^H) \quad (12)$$

$$\partial_t \bar{P}_k^E = \bar{M}_k^{-1} (\bar{M}_k^{\kappa^{-1}} \bar{E}_k - \bar{M}_k^d \bar{P}_k^E) \quad (13)$$

where  $\bar{H}_k$ ,  $\bar{E}_k$ ,  $\bar{P}_k^H$ , and  $\bar{P}_k^E$  are vectors composed of the unknown coefficients to be solved for,  $\bar{M}_k$  and  $\bar{M}_k^\alpha$ ,  $\alpha = a, b, c, d, \kappa^{-1}$ , are mass matrices

$$\bar{M}_k(i, j) = \int_{\Omega_k} \ell_i(\mathbf{r}) \ell_j(\mathbf{r}) d\mathbf{r} \quad (14)$$

$$\bar{M}_k^{\alpha, u}(i, j) = \int_{\Omega_k} \alpha_{uu}(\mathbf{r}) \ell_i(\mathbf{r}) \ell_j(\mathbf{r}) d\mathbf{r} \quad (15)$$

$\bar{\mathbb{C}}_k(f_k, f_{k'}, g_k, g_{k'})$  denotes the curl operator

$$\bar{\mathbb{C}}_k^u(f_k, f_{k'}, g_k, g_{k'}) = \bar{S}_k^v f_k^w - \bar{S}_k^w f_k^v + \bar{F}_k \mathbb{F}^u(f_k, f_{k'}, g_k, g_{k'})$$

where  $u \in \{x, y, z\}$ ,  $(f, g) \in \{(\bar{E}, \bar{H}), (\bar{H}, \bar{E})\}$ ,  $\mathbb{F}$  is the numerical flux, which in general involves unknowns from the current element  $k$  and its neighboring element  $k'$  [8], [21], [22],  $\bar{S}_k$  and  $\bar{F}_k$  are stiffness and face mass matrices defined as

$$\bar{S}_k^u(i, j) = \int_{\Omega_k} \ell_i(\mathbf{r}) \frac{d\ell_j(\mathbf{r})}{du} d\mathbf{r} \quad (16)$$

$$\bar{F}_k(i, j) = \oint_{\partial\Omega_k} \ell_i(\mathbf{r}) \ell_j(\mathbf{r}) d\mathbf{r} \quad (17)$$

respectively,  $\varepsilon_k$  and  $\mu_k$  are constant in each element. Here, the nodal DG framework [8] is used. But the proposed method can be directly applied to vector DG methods [6], [9], [23] as well. In the above definitions,  $\ell_i(\mathbf{r})$ ,  $i = 1, \dots, N_p$ , are Lagrange polynomials [8],  $\Omega_k$  and  $\partial\Omega_k$  denote the volume and surface of each element, respectively,  $k = 1, \dots, K$ ,  $N_p = (p+1)(p+2)(p+3)/6$  is the number of interpolating nodes,  $p$  is the order of the Lagrange polynomials.

Consider linear elements, the mass matrix  $\bar{M}_k$  in (14) is simply a scaled version of the mass matrix  $\bar{M}$  defined on the reference element,  $\bar{M}_k = J_k \bar{M}$ , where  $J_k$  is the Jacobian of the affine mapping between element  $k$  and the reference element. Hence, only  $\bar{M}$  and the constant  $J_k$  need to be stored in memory. Similarly, in (15), if the coefficients are EC,  $\alpha_{uu}(\mathbf{r}) = \alpha_{uu}^k$  in element  $k$ , and  $\bar{M}_k^{\alpha, u} = \alpha_{uu}^k \bar{M}_k = \alpha_{uu}^k J_k \bar{M}$ . In this case, (10)-(13) can be implemented efficiently as the case without PML [8].

However, if  $\alpha_{uu}$  varies inside the element,  $(\bar{M}_k^{\alpha, u})$ 's are different in different elements and in general there is no simple relationship between mass matrices of different elements. One has to store one copy of this mass matrix (or its inverse) for each element. Otherwise, the mass matrix needs to be calculated at each time step, which would cost a lot more computation [8]. The memory-cost for storing the mass matrices  $(\bar{M}_k^{\alpha, u})$ 's in (10)-(13) is  $3 \times 5 \times N_p^2$  floating-point numbers per each element, where 3 comes from the  $(x, y, z)$  components of the vector field, 5 comes

from the coefficients  $a(\mathbf{r})$ ,  $b(\mathbf{r})$ ,  $c(\mathbf{r})$ ,  $d(\mathbf{r})$ , and  $\kappa(\mathbf{r})$ . Note that this memory-cost is significantly higher than that of storing the unknowns of each element, where the latter is  $12 \times N_p$  in the PML region.

To reduce the memory-cost of implementing (15), we use the WAA proposed in [18]. It has been shown that with this approximation DG retains provable energy-stability and high-order accuracy [18]–[20]. It should be noted that in the SC-PML formulation (5)-(6), directly multiplying  $\ddot{a}^{-1}$  on both sides can reduce the number of element-dependent mass matrices to 4. But it would result in a non-conservative form, which may cause instability and is difficult to prove the high-order accuracy of DGTD [8], [18].

First, a weight-adjusted inner product is introduced to approximate the parameter-weighted inner product of the mass matrix [18]. The mass matrix of element  $k$  associated with locally varying coefficient  $\alpha$  is approximated as

$$\bar{M}_k^\alpha \approx \bar{M}_k (\bar{M}_k^{1/\alpha})^{-1} \bar{M}_k. \quad (18)$$

Since  $(\bar{M}_k^\alpha)^{-1}$  is directly used in (10)-(13) (for  $\alpha = a$ ), one needs to calculate  $\bar{M}_k^{1/\alpha}$ . Under the nodal DG framework [8],

$$\begin{aligned} (\bar{M}_k^{1/\alpha})_{ij} &= J_k \int_{\Omega_k} \alpha^{-1}(\mathbf{r}) \ell_i(\mathbf{r}) \ell_j(\mathbf{r}) d\mathbf{r} \\ &\approx J_k \sum_q \ell_i(\mathbf{r}_q) w_q \alpha_k^{-1}(\mathbf{r}_q) \ell_j(\mathbf{r}_q) \end{aligned} \quad (19)$$

where  $\mathbf{r}_q$ ,  $q = 1, \dots, N_q$ , are Gaussian quadrature nodes corresponding to quadrature degree  $2p + 1$ ,  $w_q$  are the corresponding weights. Hence,

$$\bar{M}_k^{1/\alpha} = J_k \bar{V}_q^T \bar{w}_q \bar{\alpha}_k^{-1} \bar{V}_q \quad (20)$$

where  $\bar{V}_q$  is an interpolation matrix defined on the reference element,  $\bar{V}_q = \bar{V}_I \bar{V}^{-1}$ ,  $\bar{V}_I$  and  $\bar{V}$  are generalized Vandemonde matrices defined as  $(\bar{V}_I)_{qi} = \phi_i(\mathbf{r}_q)$  and  $\bar{V}_{ji} = \phi_i(\mathbf{r}_j)$ , respectively,  $\phi_i(\mathbf{r})$  is the  $i$ -th orthonormal polynomial basis [8],  $\bar{w}_q = \text{diag}\{w_1, \dots, w_{N_q}\}$  is also element-independent, and  $\bar{\alpha}_k^{-1} = \text{diag}\{\alpha_k^{-1}(\mathbf{r}_1), \dots, \alpha_k^{-1}(\mathbf{r}_{N_q})\}$  is a diagonal matrix containing the coefficients evaluated at the quadrature nodes.

Inverting (18) and substituting (20) gives

$$\begin{aligned} (\bar{M}_k^\alpha)^{-1} &\approx \bar{M}_k^{-1} (\bar{M}_k^{1/\alpha}) \bar{M}_k^{-1} \\ &= \bar{M}_k^{-1} \bar{V}_q^T \bar{w}_q \bar{\alpha}_k^{-1} \bar{V}_q \bar{M}_k^{-1} \\ &= \bar{P}_q \bar{\alpha}_k^{-1} \bar{V}_q \bar{M}_k^{-1}. \end{aligned} \quad (21)$$

Here,  $\bar{P}_q \equiv \bar{M}_k^{-1} \bar{V}_q^T \bar{w}_q$  is introduced to simplify the implementation. In (21),  $\bar{P}_q$  and  $\bar{V}_q$  are defined on the reference element,  $\bar{M}_k^{-1}$  is a scaled version of the reference matrix,  $\bar{M}_k^{-1} = J_k^{-1} \bar{M}^{-1}$ .

Further on, the update equations (10)-(13) contain multiplications between element-dependent mass matrices. To reduce the number of mathematical operations, the following operators are defined

$$\tilde{M}_k^b = (\bar{M}_k^a)^{-1} \bar{M}_k^b = \bar{P}_q \bar{\alpha}_k^{-1} \bar{V}_q \bar{P}_q \bar{b}_k \bar{V}_q \quad (22)$$

$$\tilde{M}_k^c = (\bar{M}_k^a)^{-1} \bar{M}_k^c = \bar{P}_q \bar{\alpha}_k^{-1} \bar{V}_q \bar{P}_q \bar{c}_k \bar{V}_q \quad (23)$$

$$\tilde{M}_k^d = \bar{M}_k^{-1} \bar{M}_k^d = \bar{P}_q \bar{d}_k \bar{V}_q \quad (24)$$

$$\tilde{M}_k^{1/\kappa} = \bar{M}_k^{-1} \bar{M}_k^{1/\kappa} = \bar{P}_q \bar{\kappa}_k^{-1} \bar{V}_q \quad (25)$$

where (21) is used for  $\alpha = a$  and (20) is used for  $\alpha = b, c, d, \kappa^{-1}$ . These operators can be directly used on the right hand sides of (10)-(13). Substituting (22)-(25) into (10)-(13) yields

$$\partial_t \bar{H}_k = -\bar{P}_q \bar{a}_k^{-1} \bar{V}_q [\bar{P}_q (\bar{b}_k \bar{V}_q \bar{H}_k + \bar{c}_k \bar{V}_q \bar{P}_k^H) + \mu_k^{-1} \bar{\mathbb{C}}_k(\bar{E}_k, \bar{E}_{k'}, \bar{H}_k, \bar{H}_{k'})] \quad (26)$$

$$\partial_t \bar{H}_k = -\bar{P}_q \bar{a}_k^{-1} \bar{V}_q [\bar{P}_q (\bar{b}_k \bar{V}_q \bar{H}_k + \bar{c}_k \bar{V}_q \bar{P}_k^H) - \epsilon_k^{-1} \bar{\mathbb{C}}_k(\bar{H}_k, \bar{H}_{k'}, \bar{E}_k, \bar{E}_{k'})] \quad (27)$$

$$\partial_t \bar{P}_k^H = \bar{P}_q (\bar{\kappa}_k^{-1} \bar{V}_q \bar{H}_k - \bar{d}_k \bar{V}_q \bar{P}_k^H) \quad (28)$$

$$\partial_t \bar{P}_k^H = \bar{P}_q (\bar{\kappa}_k^{-1} \bar{V}_q \bar{H}_k - \bar{d}_k \bar{V}_q \bar{P}_k^H). \quad (29)$$

Equations (26)-(29) can be implemented in a matrix-free manner as in the classical DG implementation [8]. Comparing with (10)-(13), one can see that the requirement of storing the local mass matrices in (26)-(29) reduces to storing the locally varying coefficients.

### B. Computational complexity

In DGTD with explicit time iteration, the operations are element-wise. The computational cost in the PML region is  $K_{\text{PML}}$  times the cost of a single element. The memory-cost for the mass matrices in the direction implementation of (10)-(13) is  $K_{\text{PML}} \times 15N_p^2$  FPNs for the 15 component-wise coefficients. In the WAA formulation (26)-(29), the memory-cost reduces to  $(K_{\text{PML}} \times 15N_q) + 2N_p N_q$  FPNs, where  $15N_q$  comes from the 15 component-wise coefficients evaluated at the quadrature points and  $2N_p N_q$  comes from  $\bar{V}_q$  and  $\bar{P}_q$  defined on the reference element. In practice,  $N_q \sim N_p$  for simplicial quadratures that are exact for polynomials of degree  $2p + 1$  [24], [25].

To compare the arithmetic operations, one should note that the curl operator  $\bar{\mathbb{C}}$  is the same in both formulations.  $\bar{\mathbb{C}}$  involves calculations of the spatial derivatives and the numerical flux, in which the memory-access time is significant because of requiring data of neighboring elements that are discontinuous in memory. Such that the number of arithmetic operations for this term is less meaningful. Hence, only the operations of the remaining terms are compared. For the same reason, in practice, the  $\bar{\mathbb{C}}$  operator dominates the computational time, the difference in arithmetic operations estimated below based on the remaining terms is less significant (see the example in the next section).

In (10), the three matrix-vector multiplications and two vector-vector additions require  $3N_p^2$  multiplication operations and  $2N_p$  addition operations, respectively. In (26), the multiplication of  $\bar{V}_q$  with a vector of length  $N_p$ , and the multiplication between  $\bar{P}_q$  and a vector of length  $N_q$  require  $N_q N_p$  multiplication operations. The multiplication of a diagonal matrix with a vector, such as  $\bar{b}_k \bar{v}$ , takes  $N_q$  multiplication operations. Hence, excluding the  $\bar{\mathbb{C}}$  operator, (26) requires  $5N_q N_p + 3N_q$  multiplications and  $N_q + N_p$  additions. For the auxiliary variable, the cost of (12) is  $3N_p^2$  multiplications and  $N_p$  subtractions, while (28) requires  $3N_q N_p + 2N_q$  multiplications and  $N_q$  subtractions. One can see the number of operations in the WAA implementation is slightly higher than that in the direct implementation.

### III. EXAMPLES

The accuracy and efficiency of the proposed WAA formulation are compared to those of the traditional PML implementations. First, we consider the reflection of a plane wave normally impinges on the PML. To test the PML performance, perfect electric conductor (PEC) boundary conditions are used at the end of the PML and periodic boundary conditions are used in the transverse directions. The domain is filled with air with length 60 cm and the PML thickness is 1.6 cm. The mesh size (edge length) is 0.4 cm. A plane wave source is located at the center of the computation domain. The excitation signal is a Gaussian pulse  $s(t) = e^{(t-t_0)^2/4\tau^2}$ , where  $\tau = 66.67$  ps and  $t_0 = 15\tau$ . The domain is long enough such that the reflected signal is well-separated from the incident signal. Then, the reflection from the PML is simply measured from the peak of the reflected signal.

Consider the three configurations shown in Fig. 1, i.e., (a) a EC profile with a simple paved mesh, (b) a EC profile with a layered mesh, and (c) a SV profile with a paved mesh. The conductivity function is  $\sigma_u(u) = \sigma_{max}[(u - u_i)/L_{u_i}]^{p_\sigma}$ ,  $u \in \{x, y, z\}$ ,  $u_i \in \{x_i^\pm, y_i^\pm, z_i^\pm\}$ , where  $u_i$  is the  $u$ -coordinate on the interface between PML and the solution-domain in the  $u_i$ -direction,  $L_{u_i}$  is the thickness of the PML attaching to  $u_i$ , and  $\sigma_u(u)$  is nonzero only when  $|u| > |u_i|$  in the corresponding direction. Here,  $z_i^\pm = \pm 30$  cm,  $x_i^\pm = y_i^\pm = \pm\infty$ ,  $p_\sigma = 1$ , and  $L_{z_i^\pm} = 1.6$  cm. For the SV case  $z$  is taken as the  $z$ -coordinate of each node and for the EC case  $z$  is set as the  $z$ -coordinate of the vertex farthest away from the PML interface in the element where the node resides in.  $\kappa = 1$

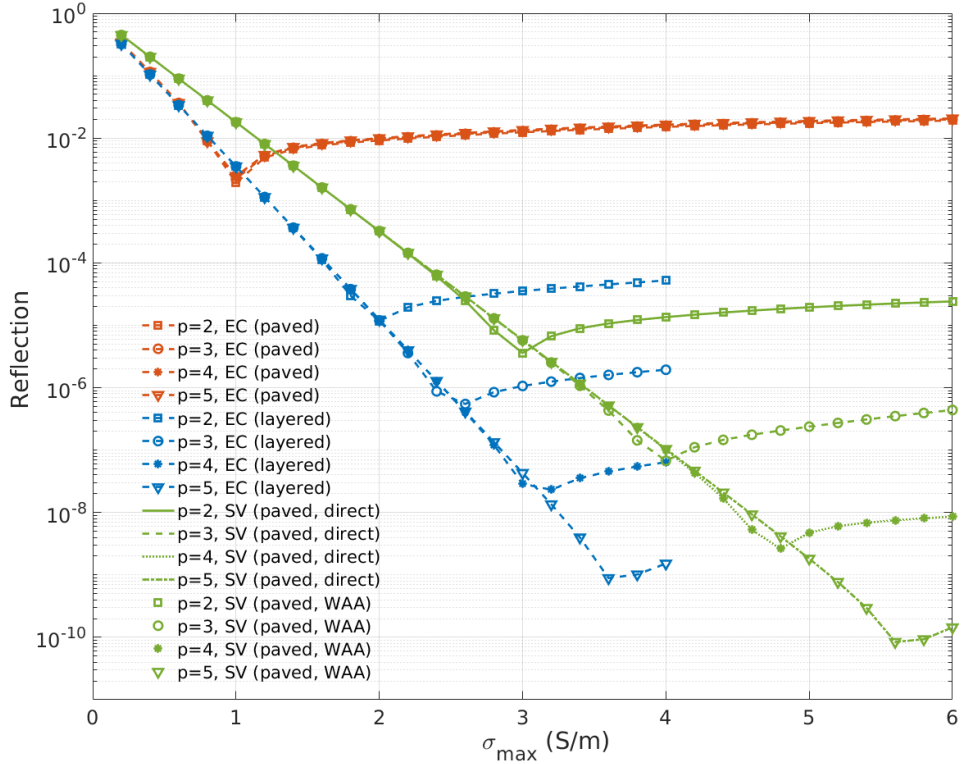


Fig. 2. Reflection of a plane wave normally incident on PMLs of different configurations/implementations.

in this example.

For each configuration  $\sigma_{max}$  is scanned to find the minimal reflection that could be reached. Fig. 2 shows, as increasing  $\sigma_{max}$ , the reflection first decreases exponentially and then increases gradually. This is an universal behavior for all configurations. When  $\sigma_{max}$  is small, the reflection is dominated by the PEC boundary at the end of the PML, because of lacking enough absorption. As increasing  $\sigma_{max}$ , the wave amplitude returning back to the solution domain decreases exponentially. Meanwhile, the numerical reflection, which stems from discretization, increases as increasing  $\sigma_{max}$  [11]. After reaching a minimal point, the numerical reflection starts to dominate.

The WAA implementation and the direct implementation (using local mass matrices) are compared in case (c). The quadrature order is chosen as  $2p$ . For  $p = 1, 2, 3, 4, 5$ ,  $N_p = 4, 10, 20, 35, 56$  and  $N_q = 4, 11, 23, 44, 74$  [25]. Fig. 2 shows the WAA implementation performs exactly the same as the direct implementation, which verifies the accuracy of the proposed formulation. One can also see the SV profile outperforms the EC profiles. For case (a), the reflection stays at a high level and does not decrease as increasing the polynomial order  $p$ . This is because of the reflection at those unoriented internal interfaces. Probably this is one reason that it was observed that a constant conductivity performs even better than polynomial conductivity profiles in [17]. Both case (b) and case (c) show high-order accuracy, i.e., the minimal reflection decreases exponentially as increasing  $p$ . Still, the minimal reflection with the SV profile is about 15 dB smaller than that of the layered EC profile.

Next, consider the wave scattering from a PEC sphere. The simulation domains for the EC and SV cases are shown in Fig. 3 (a) and (b), respectively. The radius of the sphere is 1 cm.  $x_i^\pm = y_i^\pm = z_i^\pm = \pm 2.2$  cm, and  $L_{x_i^\pm} = L_{y_i^\pm} = L_{z_i^\pm} = 1.2$  cm. The background material is air. A plane wave is excited from the total-field scattering-field interface and impinges on the PEC sphere. The excitation signal is the same as before. Because of the small distance between the sphere surface and the PML interface, the scattered waves enter the PML with

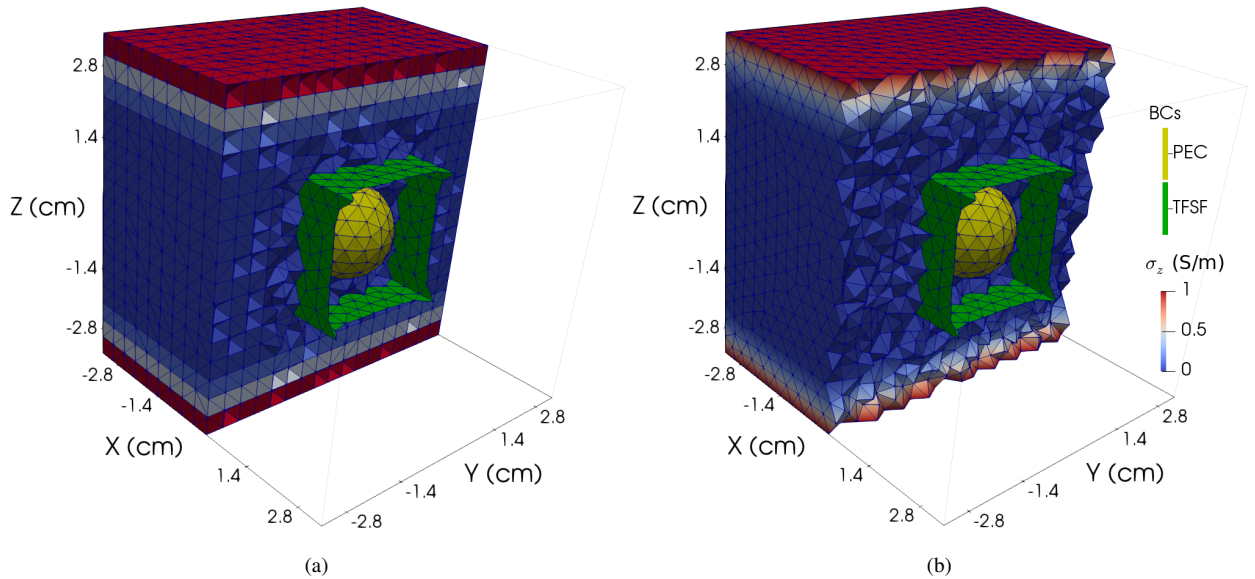


Fig. 3. Computation domains, meshes, and PML conductivity profiles used for the (a) layered EC and (b) paved SV configurations.



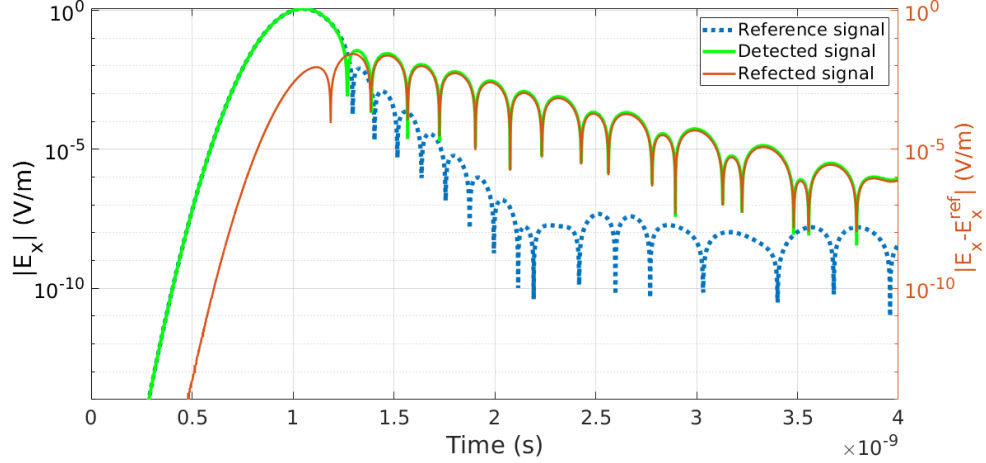


Fig. 4. Electric field signals calculated from the reference and the testing configurations. The reflection is calculated from the maximal absolute difference between those two signals.

high grazing angles and evanescent waves also enter the PML. A varying  $\kappa$  profile is employed to help absorbing evanescent waves [12], [13]:  $\kappa_u(u) = 1 + (\kappa_{max} - 1)[(u - u_i)/L_{u_i}]^{p_\kappa}$ , where  $p_\kappa = p_\sigma$  and  $\kappa_{max} = 2$  are used. Inside the solution domain  $\kappa = 1$ . In this example, using the PEC or the first-order absorbing boundary condition [14] at the outermost boundary gives similar results. The results below are obtained with the PEC boundary condition.

In the EC case, to ensure the material interfaces are strictly parallel to the axes, virtual boxes are built layer by layer (to control meshes) and  $\sigma_u$  and  $\kappa_u$  values in each layer are set manually using the  $u$ -coordinate on the boundary at the far-end of the layer in the  $u_i$ -direction. Each layer has thickness 0.4 cm. This process is tedious since in the corner region one has to align all material interfaces in all three directions. In contrast, in the SV case,  $\sigma_u$  and  $\kappa_u$  values are simply set according the coordinates of each node. The pre-processing is simplified a lot since even an explicit interface between the simulation domain and PML is not required [Fig. 3 (b)].

The reference scattered signals are calculated with the same source and scatter as those of the testing cases but the distance between the sphere surface and the PML is extended to 12 cm. To ensure the discretization errors are at the same level in the testing and the reference configurations, the meshes in the overlapped region are kept the same and the mesh size in the extended region of the reference configuration is kept the same.

Fig. 4 shows the electric field signals recorded at (1 cm, 1 cm, 0). The reflected signal is the absolute difference between the signals of the testing and the reference configurations. The reflection is measured from the peak of the reflected signal.  $\sigma_{max}$  is scanned to find the minimal reflection that could be reached for each configuration. Fig. 5 shows the results. Clearly, the SV profile performs better than the layered EC profile for each  $p_\sigma$ . The best performance is obtained at  $p_\sigma = 2$  in this example. Further increasing  $p_\sigma$  degrades the PML performance since high conductivity values only appear at the very end of the PML when  $p_\sigma$  is high.

Fig. 5 also shows that the WAA implementation performs exactly the same as the direct implementation, which means the error caused by the WAA of the mass matrices is below the discretization error (which limits the PML performance). Table. I compares the computational cost of the WAA and direct implementations. As increasing the

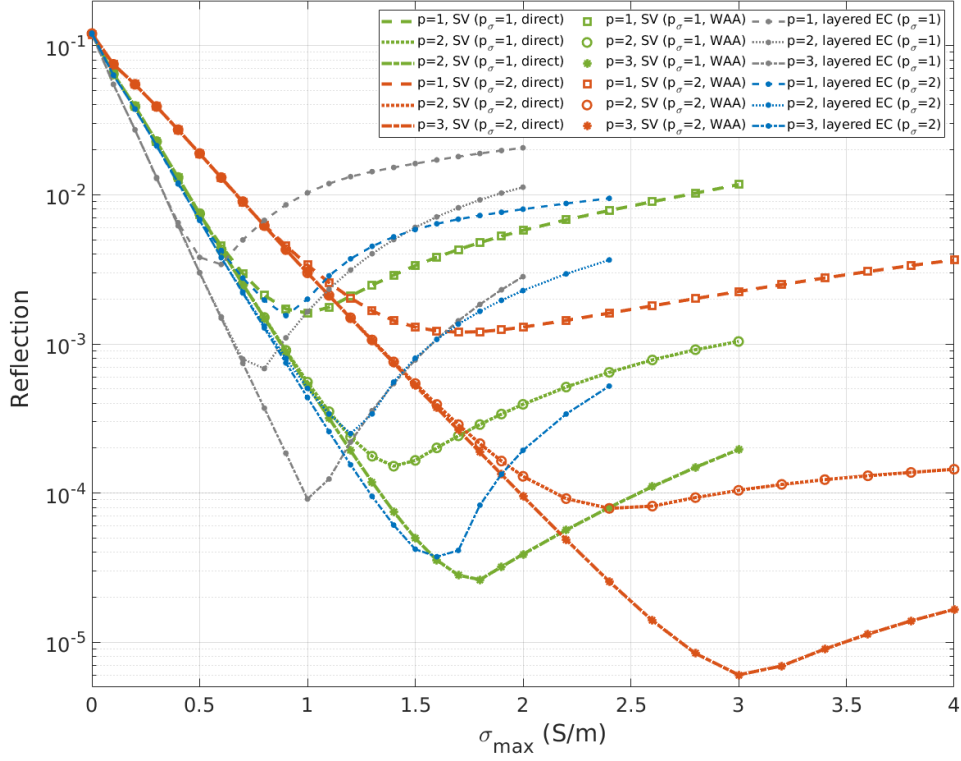


Fig. 5. Reflection of the wave scattered from a PEC sphere calculated with different PML configurations/implementations.

order of the polynomial basis functions, the memory cost increases dramatically in the direction implementation but modestly in the WAA implementation. For  $p = 5$ , the memory cost of the direct implementation is 12.4 times that of the WAA implementation. Meanwhile, the CPU time per iteration in the WAA implementation is slightly larger than that in the direct implementation, due to the increased arithmetic operations (see Section. II-B). In practice, a DGTD algorithm is usually parallelized. The small difference of CPU time for updating different elements can be

TABLE I  
COMPUTATIONAL COSTS OF DIRECT AND WAA IMPLEMENTATIONS\*.

$p$	$N_p$	memory (KB)		CPU time per step (s)	
		direct	WAA	direct	WAA
1	4	378,660	267,928	1.652716	2.341525
2	10	1,274,424	498,508	4.083981	5.960960
3	20	4,126,640	894,936	9.606642	15.73330
4	35	11,583,440	1,513,140	19.64900	30.16986
5	56	28,410,000	2,291,608	78.56877	105.1317

\* Tested on a workstation with Intel Xeon(R) E5-2680 v4 CPU and 128GB memory. A single process is used.  $K = 72, 762$  and  $K_{\text{PML}} = 52, 657$ .

easily compensated by allocating a smaller number of elements for those MPI processes containing PML elements. From our tests, assigning a weight of 2 for PML elements in ParMetis [26] could reach a good load-balance.

#### IV. CONCLUSION

In summary, a low-memory implementation of PML with smooth-varying coefficients in DGTD is proposed. Employing a smooth-varying profile in PML equips with advantages that a smaller numerical reflection of PML could be reached and the meshing process can be greatly simplified (mesh interfaces are not required to be parallel to the axes). It has been shown that the proposed implementation dramatically reduces the memory-cost without sacrificing the accuracy (in terms of the PML reflection) as compared to the direct implementation, while its computational time increases modestly. This memory-efficient implementation is very useful for solvers running on share-memory systems where the high-memory cost of smooth-varying PMLs could be a bottleneck. For distributed-memory systems, the memory requirement of a single computing node is also reduced and a better load-balance could be reached with a slightly adjusted weight in the domain partition.

#### REFERENCES

- [1] J.-P. Berenger, "A perfectly matched layer for the absorption of electromagnetic waves," *J. Comput. Phys.*, vol. 114, no. 2, pp. 185–200, 1994.
- [2] W. C. Chew and W. H. Weedon, "A 3D perfectly matched medium from modified Maxwell's equations with stretched coordinates," *Microw. Opt. Tech. Lett.*, vol. 7, no. 13, pp. 599–604, 1994.
- [3] A. Taflov and S. C. Hagness, *Computational electrodynamics: the finite-difference time-domain method*. Artech house, 2005.
- [4] J.-M. Jin, *The finite element method in electromagnetics*. John Wiley & Sons, 2015.
- [5] J. Hesthaven and T. Warburton, "Nodal high-order methods on unstructured grids: I. time-domain solution of Maxwell's equations," *J. Comput. Phys.*, vol. 181, no. 1, pp. 186 – 221, 2002.
- [6] B. Cockburn, F. Li, and C.-W. Shu, "Locally divergence-free discontinuous Galerkin methods for the Maxwell equations," *J. Comput. Phys.*, vol. 194, no. 2, pp. 588 – 610, 2004.
- [7] T. Lu, P. Zhang, and W. Cai, "Discontinuous Galerkin methods for dispersive and lossy Maxwell's equations and PML boundary conditions," *J. Comput. Phys.*, vol. 200, no. 2, pp. 549–580, 2004.
- [8] J. Hesthaven and T. Warburton, *Nodal Discontinuous Galerkin Methods: Algorithms, Analysis, and Applications*. NY, USA: Springer, 2008.
- [9] S. D. Gedney, C. Luo, J. A. Roden, R. D. Crawford, B. Guernsey, J. A. Miller, T. Kramer, and E. W. Lucas, "The discontinuous Galerkin finite-element time-domain method solution of Maxwell's equations," *Appl. Comput. Electromagn. Soc. J.*, vol. 24, no. 2, p. 129, 2009.
- [10] G. C. Cohen and S. Pernet, *Finite element and discontinuous Galerkin methods for transient wave equations*. Springer, 2017.
- [11] W. C. Chew and J. Jin, "Perfectly matched layers in the discretized space: An analysis and optimization," *Electromagn.*, vol. 16, no. 4, pp. 325–340, 1996.
- [12] J.-P. Berenger, "Perfectly matched layer (PML) for computational electromagnetics," *Synthesis Lectures on Computational Electromagnetics*, vol. 2, no. 1, pp. 1–117, 2007.
- [13] S. D. Gedney, "Introduction to the finite-difference time-domain (fdtd) method for electromagnetics," *Synthesis Lectures on Computational Electromagnetics*, vol. 6, no. 1, pp. 1–250, 2011.
- [14] L. Angulo, J. Alvarez, M. Pantoja, S. Garcia, and A. Bretones, "Discontinuous Galerkin time domain methods in computational electrodynamics: State of the art," in *Forum Electromagn. Res. Methods Appl. Technol.*, vol. 10, 2015, pp. 1–24.
- [15] L. M. D. Angulo, "Time domain discontinuous Galerkin methods for Maxwell equations," Ph.D. dissertation, Universidad de Granada, 2014.
- [16] K. Sankaran, "Accurate domain truncation techniques for time-domain conformal methods," Ph.D. dissertation, ETH Zurich, 2007.

- [17] J. Niegemann, M. König, K. Stannigel, and K. Busch, “Higher-order time-domain methods for the analysis of nano-photonic systems,” *Photonic. Nanostruct.*, vol. 7, no. 1, pp. 2–11, 2009.
- [18] J. Chan, R. J. Hewett, and T. Warburton, “Weight-adjusted discontinuous Galerkin methods: wave propagation in heterogeneous media,” *SIAM J. Sci. Comput.*, vol. 39, no. 6, pp. A2935–A2961, 2017.
- [19] K. Guo and J. Chan, “Bernstein-Bezier weight-adjusted discontinuous Galerkin methods for wave propagation in heterogeneous media,” *J. Comput. Phys.*, vol. 400, p. 108971, 2020.
- [20] K. Shukla, J. Chan, V. Maarten, and P. Jaiswal, “A weight-adjusted discontinuous galerkin method for the poroelastic wave equation: penalty fluxes and micro-heterogeneities,” *J. Comput. Phys.*, vol. 403, p. 109061, 2020.
- [21] L. Chen and H. Bagci, “Steady-state simulation of semiconductor devices using discontinuous Galerkin methods,” *IEEE Access*, vol. 8, pp. 16 203–16 215, 2020.
- [22] L. Chen and H. Bagci, “Multiphysics modeling of plasmonic photoconductive devices using discontinuous Galerkin methods,” *arXiv preprint arXiv:1912.03639*, 2019.
- [23] P. Li, L. J. Jiang, and H. Bagci, “A resistive boundary condition enhanced DGTD scheme for the transient analysis of graphene,” *IEEE Trans. Antennas Propag.*, vol. 63, no. 7, pp. 3065–3076, July 2015.
- [24] R. Cools, “Monomial cubature rules since “stroud”: A compilation – part 2,” *J. Comput. Appl. Math.*, vol. 112, no. 1-2, pp. 21–27, Nov. 1999.
- [25] H. Xiao and Z. Gimbutas, “A numerical algorithm for the construction of efficient quadrature rules in two and higher dimensions,” *Comput. Math. with Appl.*, vol. 59, no. 2, pp. 663–676, 2010.
- [26] G. Karypis and V. Kumar, “A parallel algorithm for multilevel graph partitioning and sparse matrix ordering,” *Journal of Parallel and Distributed Computing*, vol. 48, no. 1, pp. 71–95, 1998.